Percolation versus depinning transition: The inherent role of damage hardening during quasibrittle failure

Ashwij Mayya

Percolation versus depinning transition : The inherent role of damage hardening during quasibrittle failure

Ashwij Mayya*
Institut Jean Le Rond D'Alembert (UMR 7190), Sorbonne Université & CNRS, Paris, France
(Dated: September 24, 2024)

The intermittent damage evolution preceding the failure of heterogeneous brittle solids is well described by scaling laws. In deciphering its origins, failure is routinely interpreted as a critical transition. However at odds with expectations of universality, a large scatter in the value of the scaling exponents is reported during acoustic emission experiments. Here we numerically examine the precursory damage activity to reconcile the experimental observations with critical phenomena framework. Along with the strength of disorder, we consider an additional parameter that describes the progressive damageability of material elements at mesoscopic scale. This hardening behavior encapsulates the micro-fracturing processes taking place at lower length scales. We find that damage hardening can not only delay the final failure, but also affect the preceding damage accumulation. When hardening is low, the precursory activity is strongly influenced by the strength of the disorder and is reminiscent of damage percolation. On the contrary, for large hardening, long-range elastic interactions prevail over disorder, ensuring a rather homogeneous evolution of the damage field in the material. The power-law statistics of the damage bursts is robust to the strength of the disorder, and is reminiscent of the collective avalanche dynamics of elastic interfaces near the depinning transition. The existence of these two distinct universality classes also manifests as different values of the scaling exponent characterizing the divergence of the precursor size on approaching failure. Our finding sheds new light on the connection between the level of quasi-brittleness of materials and the statistical features of the failure precursors. Finally, it also provides a more complete description of the acoustic precursors and thus paves the way for quantitative techniques of damage monitoring of structures-in-service.

I. INTRODUCTION

Failure of heterogeneous solids takes place through intermittent bursts of localized damage activity [1–3]. The acoustic emissions accompanying the precursory activity are scale-invariant. The source-map of such events reveals a progressively coherent spatial and temporal distribution of events that finally localize along a plane at failure [4, 5]. They assert the collective nature of damage growth in heterogeneous solids. And yet, apart from the presence of power laws, a comprehensive understanding of the precursory damage accumulation remains elusive. Consequently, the connection of precursors with the final failure itself, is also not clear.

The scale-free statistics of precursors strongly argue for an interpretation of failure as a critical phenomenon [6–13]. Indeed, both energy and frequency of acoustic hits accompanying damage evolution of brittle solids are shown to increase on approaching failure in the literature. However, a careful examination of the experimental data reveals that such an interpretation may not be straightforward [14]. In particular, the exponent $\alpha_{N_{\rm AE}}$ describing the increase, $dN_{\rm AE}/dt \sim |t_{\rm c} - t|^{-\alpha_{N_{\rm AE}}}$ of the activity rate $dN_{\rm AE}/dt$ close to failure at time $t_{\rm c}$ displays a wide-range of values. During compressive failure, values ranging from 0.5 upto 0.75 are reported in case of synthetic SiO_2 and rocks [10, 15–17], concrete [13], and $\alpha_{N_{\rm AE}} \simeq 1.0$ is reported for complex materials such as shale [15] and teeth [18]. For tensile failure, the value of $\alpha_{N_{\rm AE}}$ is even higher : 1.4 for un-notched specimens of paper during uniaxial tension tests [11], 1.68 and 1.28 for specimens of bamboo chopsticks [19] and marble [20], respectively during three-point bending tests [21]. Such a scatter is at odds with the expectations of an universal exponent, a hall-mark of critical phenomena. Even the exponent $\tau_{\rm AE}$ characterizing the distribution of the energies of the acoustic emissions, $P(E_{\rm AE}) \sim E_{\rm AE}^{-\tau_{\rm AE}}$ is found to vary from 1.3 upto 1.8 in experiments involving different brittle solids [6–11, 13–19, 22].

Independent of the experiments, numerical studies of fracture that focus on the interplay of the disorder and the elastic interactions, routinely consider an assembly of brittle elements with randomly distributed thresholds [23–35]. Damage evolution in such phenomenological models corresponds to a series of correlated breakage events. As a result, except for weak disorder, failure is preceded by scale-invariant damage activity [30, 31]. Surprisingly, these observations have been interpreted as a signature of both discontinuous (first-order) and continuous (second-order) transitions. In the first case, the seemingly critical aspects of precursors are attributed to the sweeping of an instability [25–27, 32, 36]. Whereas in the second case, a scenario of percolation transition is proposed [23, 28, 31, 34]. In addition to the strength of disorder, the functional form of the elastic interactions is also shown to affect the results of these numerical models [34, 37–39]. Rationalizing these numerical observations in relation to the experiments is therefore rather difficult.

To reconcile the various contrasting interpretations, we recently proposed a framework for capturing the co-

* ashwijmayya@gmail.com

operative dynamics of precursory damage evolution during compressive failure of disordered solids [40, 41]. The elastic interactions were described explicitly by deriving a non-local theory of continuum damage mechanics relying on a rigorous description of the redistribution of elastic energy release rate during the heterogeneous growth of the damage field [42–44]. It revealed a profound connection between the intermittent dynamics of damage evolution and the out-of-equilibrium physics of disordered systems - The precursory damage activity was shown to be reminiscent of the depinning dynamics of a non-standard driven elastic interface [45, 46]. At the same time, the evolution toward failure was described by the non-stationary evolution of the interface culminating in a loss of stability. As a result, the salient features of the precursory activity namely, the size, the spatial extent and the duration were described by critical exponents, reminiscent of depinning transition. On the contrary, the power law divergence on approaching failure was shown to be the signature of a standard bifurcation in the damage evolution. Interestingly, a combination of these two phenomena provided numerous time-to-failure scaling laws that are useful for predicting failure from precursors [47].

A subtle but important aspect of the proposed framework was the consideration of damage hardening at the local scale. In presence of hardening, mesoscopic scale elements are assigned a *ductile* response and the damage evolution is rather homogeneous. This behavior is in good agreement with various experimental observations [48–54]. However, the extent of hardening may vary with materials. Also, several experiments may present a relatively short precursory damage accumulation phase corresponding to low hardening, especially during traction tests. The objective of our work is therefore the following. *What is the connection between hardening and material's failure behavior, particularly the statistics of the failure precursors ?* Such an understanding may be relevant in engineering applications - for the anticipation of failure from precursor statistics. Here we numerically examine the failure of brittle disordered solids following the proposed damage mechanics framework [40, 41]. We examine the failure behavior for different values of damage hardening and strength of disorder, and obtain the following main results:

- Hardening plays a key role during quasi-brittle failure. In presence of large hardening, we observe scale-free statistics even for weakly disordered solids, an observation that is at odds with standard models where a brittle constitutive response is considered at the local level (see *e.g.*, [27]).

- The transition in hardening behavior from small to large presents distinctly different damage spreading modes that are dominated by disorder and elastic interactions, respectively. Strikingly, the statistical signatures of the precursory activity in the two regimes correspond to two different universality classes. When damage hardening is small, material failure is reminiscent of percolation at moderate disorder [23, 28, 30, 31]. However, when hardening is large, precursors resemble avalanche dynamics of elastic interfaces near the depinning transition [40, 41].

- The varying interpretation of precursors has implications for the nature of failure. For small damage hardening, failure corresponds to the percolation threshold, a critical point. On the contrary, damage localization appearing at the end of a prolonged intermittent damage evolution due to large damage hardening is a standard instability. This difference is highlighted in the divergence of the precursors on approaching failure. The exponent characterizing the power law divergence of precursors on approaching the percolation threshold is larger than the value measured for precursors close to localization instability.

Our findings shed light on the connection between the level of quasi-brittleness and the precursor statistics. Also, they help rationalize the wide scatter in the scaling exponents observed in acoustic emission experiments.

II. MODEL DESCRIPTION

We will now describe the theoretical framework that allowed for rationalizing the scale-free statistics of the precursors to failure during compression experiments on a model brittle disordered solid [40, 41]. It is derived using the concepts of continuum damage mechanics where the dissipation at the microscopic scale is described at a coarser level through a scalar damage variable d that takes values between 0 (intact) to 1 (failure) [55].

First, we consider the mechanical response of an isotropic elasto-damageable material during a force-controlled experiment under quasi-static loading conditions, i.e., the rate of damage evolution is much faster than the external loading rate. Therefore, the dissipation of mechanical energy occurs at a constant loading amplitude and corresponds to the loss of elastic energy in the material. To infer the evolution of damage, we then track the two energetic quantities (i) the damage driving force Y defined as the rate of elastic energy released as the damage level increases, and (ii) the critical value Y_c characterizing the material's resistance. Such an approach has been routinely used to model the quasi-brittle failure [55–57]. However, the description of the elastic interactions in the damage field in such models is rather ad-hoc, *e.g.*, considerations of a finite internal length for regularizing the damage evolution [58]. Also, such methods do not capture the intermittent nature of damage accumulation. Here we take into account the role of heterogeneities through a mesoscopic scale description of the continuum. The field $\vec{x}$ of damage is then heterogeneous. The damage level in the individual

material elements is $d(\vec{x}) = d_\circ + \delta d(\vec{x})$ where $d_\circ$ is the average damage level and $\delta d(\vec{x})$, the fluctuations around $d_\circ$. Following the elasto-damageability behavior, we infer the local elastic modulus $E[d(\vec{x})]$ to vary with the local damage level $d(\vec{x})$. Consequently, we infer a heterogeneous state of stress $\boldsymbol{\sigma}(\vec{x})$ in the material elements $\boldsymbol{\sigma}(\vec{x}) = \boldsymbol{\sigma_\circ} + \delta\boldsymbol{\sigma}(\vec{x})$. The average values in these equations denoted by the subscript $(\circ)$ are representative of the material at the macroscopic scale. The constitutive response of the disordered solid using Hooke's law then writes as

$$\boldsymbol{\epsilon} = \frac{(1+\nu)\boldsymbol{\sigma} - \nu \mathrm{Tr}(\boldsymbol{\sigma})}{E}. \tag{1}$$

Here $\boldsymbol{\epsilon}$ is the strain tensor and ν is the Poisson ratio that is taken to be a constant during damage evolution. we then obtain the elastic energy density $w(\boldsymbol{\epsilon}, \boldsymbol{\sigma}) = (1/2)\ \boldsymbol{\epsilon} \colon \boldsymbol{\sigma}$ as

$$w(\boldsymbol{\epsilon}, \boldsymbol{\sigma}) = \frac{(1+\nu)\mathrm{Tr}(\boldsymbol{\sigma}^2) - \nu \mathrm{Tr}(\boldsymbol{\sigma})^2}{2E}. \tag{2}$$

The damage driving force of the heterogeneous media at a given loading amplitude $\boldsymbol{\sigma_\circ}$ is given by

$$\begin{aligned} Y[d(\vec{x}), \boldsymbol{\sigma}] &= \left.\frac{\partial w}{\partial d_\circ}\right|_{\boldsymbol{\sigma}}, \\ &= \frac{\overline{\mu}'(d_\circ)\mathrm{Tr}(\boldsymbol{\sigma}^2)}{4} + \frac{\nu E'(d_\circ)\mathrm{Tr}(\boldsymbol{\sigma})^2}{2E(d_\circ)^2} \end{aligned} \tag{3}$$

where $\mu = E/2(1+\nu)$ is the Lamé constant and $\overline{\mu} = 1/\mu$. The prime denotes the derivative with respect to the damage variable $d_\circ$. Notably, as both the damage field $d(\vec{x})$ and the stress state in the elements $\boldsymbol{\sigma}(\vec{x})$ are heterogeneous, $Y(d_\circ, \boldsymbol{\sigma})$ can be decomposed into the average value and the fluctuations as $Y(d_\circ, \boldsymbol{\sigma}) = Y_\circ(d_\circ, \boldsymbol{\sigma_\circ}) + \delta Y(\delta d, \delta\boldsymbol{\sigma})$ where the individual terms can be expressed as the following.

$$\begin{cases} Y_\circ(d_\circ, \boldsymbol{\sigma_\circ}) &= \frac{\overline{\mu}'(d_\circ)\mathrm{Tr}(\boldsymbol{\sigma}_\circ^2)}{4} + \frac{\nu E'(d_\circ)\mathrm{Tr}(\boldsymbol{\sigma_\circ})^2}{2E(d_\circ)^2} \\ \delta Y(\delta d, \delta\boldsymbol{\sigma}) &= \left[\frac{\overline{\mu}''(d_\circ)\mathrm{Tr}(\boldsymbol{\sigma}_\circ^2)}{4} - \frac{\nu \mathrm{Tr}(\boldsymbol{\sigma_\circ})^2}{2}\left(\frac{2E'(d_\circ)^2}{E(d_\circ)^3} - \frac{E''(d_\circ)}{E(d_\circ)^2}\right)\right]\delta d(\vec{x}) + \left[\frac{\overline{\mu}'(d_\circ)\mathrm{Tr}(\boldsymbol{\sigma_\circ}\delta\boldsymbol{\sigma}(\vec{x}))}{2} + \frac{\nu E'(d_\circ)\mathrm{Tr}(\boldsymbol{\sigma_\circ})\mathrm{Tr}(\delta\boldsymbol{\sigma}(\vec{x}))}{E(d_\circ)^2}\right]. \end{cases} \tag{4}$$

In the above Eq. (4), we note that the first term of $\delta Y(\delta d, \delta\boldsymbol{\sigma})$ is solely dependent on the local fluctuations in the damage level $\delta d(\vec{x})$. On the other hand, the second term involves $\delta\boldsymbol{\sigma}(\vec{x})$ that is non-local owing to the elasticity of the damage field. As a result, the second term corresponds to the non-local component of the damage driving force. We relate the fluctuations $\delta\boldsymbol{\sigma}(\vec{x})$ to those in damage field $\delta d(\vec{x})$ using a perturbative approach [43]. In Fourier space, $\delta\tilde{\boldsymbol{\sigma}}(\vec{q}) = \frac{\overline{\mu}'(d_\circ)}{\overline{\mu}(d_\circ)}\Big[\mathbf{O}\cdot\boldsymbol{\sigma_\circ}\cdot\mathbf{O} - \nu(\mathbf{Q}\colon\boldsymbol{\sigma_\circ})\cdot\mathbf{O}\Big]\delta\tilde{d}(\vec{q})$ where the Oseen tensor $\mathbf{O} = 1 - \mathbf{Q}$ and $\mathbf{Q_{ij}} = q_i q_j/|\vec{q}|^2$. These calculations provide the non-local term of $\delta Y(\delta d, \delta\boldsymbol{\sigma})$ in terms of a Green's function $\tilde{\psi}$ in Fourier space, $\tilde{\psi}\delta\tilde{d}$. In real space, it transforms into the convolution product of $\psi(\boldsymbol{\sigma_\circ})$ with the fluctuations in the damage field $\delta d(\vec{x})$ as $\psi(\boldsymbol{\sigma_\circ}) * \delta d(\vec{x})$. Strikingly, the function $\psi(\boldsymbol{\sigma_\circ})$ depends on the boundary condition as prescribed by the macroscopic stress state $\boldsymbol{\sigma_\circ}$. Such a description of the non-local elasticity of damage field has been earlier shown to successfully explain the experimental observations of different fault orientations with the variation of boundary condition in Dansereau *et al.* [43]. The simplification of Eq. (4) therefore provides the heterogeneous damage driving force as

$$\begin{aligned} Y[d(\vec{x}), \boldsymbol{\sigma}] = Y_\circ[d_\circ, \boldsymbol{\sigma_\circ}] &+ \left.\frac{\partial Y_\circ}{\partial d_\circ}\right|_{d_\circ, \boldsymbol{\sigma_\circ}} \delta d(\vec{x}) \\ &+ \psi(\boldsymbol{\sigma_\circ}) * \delta d(\vec{x}). \end{aligned} \tag{5}$$

we note that the second and third terms of the above Eq. (5) can also be interpreted as describing the local and the non-local changes to the field of damage driving force during the homogeneous damage evolution [41].

Next, we take into account the finite loading rate v_{ext} during the force-controlled experiment. The damage field during the loading $\boldsymbol{\sigma_\circ} = \boldsymbol{\sigma_\circ}(0) + v_{\mathrm{ext}}t$ is considered to evolve as $d(\vec{x}, t) = d_\circ(0) + \Delta d(\vec{x}, t)$ where the finite incremental damage $\Delta d(\vec{x}, t) \ll d_\circ(0)$. The fluctuations in the damage field are then $\delta d(\vec{x}, t) = \Delta d(\vec{x}, t) - \langle \Delta d \rangle_{\vec{x}}$. The expression of damage driving force is given by

$$\begin{aligned} Y[d(\vec{x}, t), \boldsymbol{\sigma}] &= Y_\circ(0) + \left.\frac{\partial Y_\circ}{\partial \sigma_\circ}\right|_{d_\circ} v_{\mathrm{ext}} t + \left.\frac{\partial Y_\circ}{\partial d_\circ}\right|_{\boldsymbol{\sigma_\circ}} \Delta d(\vec{x}, t) \\ &+ \psi(\boldsymbol{\sigma_\circ}) * \left[\Delta d(\vec{x}, t) - \langle \Delta d \rangle_{\vec{x}}\right]. \end{aligned} \tag{6}$$

where we expanded the first term of Eq. (5) (upto the first order terms) to account for the finite driving rate. Similarly, keeping the heterogeneities in mind, the field of damage resistance $Y_{\mathrm{c}}(\vec{x})$ during damage evolution can

be expressed as the following.

$$Y_{\rm c}[d(\vec{x},t)] = Y_{\rm co}(d_\circ) + \left.\frac{dY_{\rm co}}{dd_\circ}\right|_{d_\circ} \delta d(\vec{x},t) + y_{\rm c}[\vec{x},d(\vec{x},t)]. \tag{7}$$

Here the first term $Y_{\rm co}(d_\circ)$ corresponds to the average value of damage resistance. Notably, it is assumed to vary with the damage level. The damage dependent variation of the material's resistance is described through the second term. Such a hardening behavior is routinely observed in experiments. Its physical origin as well as the implications on failure behavior will be discussed in detail, later in section IV of the manuscript. The third term $y_{\rm c}[\vec{x},d(\vec{x},t)]$ corresponds to the fluctuations in the damage resistance field.

Using these quantities, the generalized driving force $\mathcal{F}$ can be expressed as $\mathcal{F}[d(\vec{x},t),\boldsymbol{\sigma}] = Y[d(\vec{x},t),\boldsymbol{\sigma}] - Y_{\rm c}[d(\vec{x},t)]$. Consequently, the damage criterion writes as

$$\begin{cases} \mathcal{F} < 0 \rightarrow Y[d(\vec{x},t),\boldsymbol{\sigma}] < Y_{\rm c}[d(\vec{x},t)] : \text{stable damage}, \\ \mathcal{F} = 0 \rightarrow Y[d(\vec{x},t),\boldsymbol{\sigma}] = Y_{\rm c}[d(\vec{x},t)] : \text{damage grows}. \end{cases} \tag{8}$$

We note that Eq. (8) is analogous to the failure criterion in terms of the energy release rate that is employed in fracture mechanics [59]. Substituting Eqs. (6) and (7) into Eq. (8) provides

$$\begin{aligned} \mathcal{F}[d(\vec{x},t),\boldsymbol{\sigma}] \;=\; & \left.\tfrac{\partial Y_\circ}{\partial \boldsymbol{\sigma}_\circ}\right|_{d_\circ} v_{\rm ext} t + \left.\tfrac{\partial (Y_\circ - Y_{\rm co})}{\partial d_\circ}\right|_{\boldsymbol{\sigma}_\circ} \Delta d(\vec{x},t) + \\ & \psi(\boldsymbol{\sigma}_\circ) * [\Delta d(\vec{x},t) - \langle \Delta d \rangle_{\vec{\mathrm{x}}}] - y_{\rm c}[\vec{x},d(\vec{x},t)]. \end{aligned} \tag{9}$$

where the terms $Y_\circ(d_\circ,\boldsymbol{\sigma}_\circ)$ and $Y_{\rm co}(d_\circ)$ are equal and cancel out following the necessary equilibrium condition $\mathcal{F}_\circ(d_\circ,\boldsymbol{\sigma}_\circ) = 0$ that is satisfied at the macroscopic scale. To obtain the equation of damage evolution, we consider over-damped dynamics at small timescales [60, 61]. This provides $\Delta\dot{d}(\vec{x},t) \propto \mathcal{F}[d(\vec{x},t),\boldsymbol{\sigma}]$ where the dot represents the derivative with respect to time. Rearranging the various terms of Eq. (9), we then obtain the following evolution equation of the damage field.

$$\begin{aligned} \Delta\dot{d}(\vec{x},t) \propto \;\; & \mathcal{K}(\boldsymbol{\sigma}_\circ)\,[v_{\rm m}(\boldsymbol{\sigma}_\circ)\,t - \Delta d(\vec{x},t)] + \\ & \psi(\boldsymbol{\sigma}_\circ) * [\Delta d(\vec{x},t) - \langle \Delta d \rangle_{\vec{\mathrm{x}}}] - y_{\rm c}[\vec{x},d(\vec{x},t)], \end{aligned} \tag{10}$$

where

$$\begin{aligned} \mathcal{K}(\boldsymbol{\sigma}_\circ) &= \left.\tfrac{\partial (Y_{\rm co} - Y_\circ)}{\partial d_\circ}\right|_{\boldsymbol{\sigma}_\circ} \quad \text{and} \\ v_{\rm m}(\boldsymbol{\sigma}_\circ) &= \tfrac{\partial Y_\circ / \partial \boldsymbol{\sigma}_\circ}{\mathcal{K}(\boldsymbol{\sigma}_\circ)} v_{\rm ext}. \end{aligned} \tag{11}$$

Here $\mathcal{K}(\boldsymbol{\sigma}_\circ) = -\frac{\partial(\mathcal{F}_\circ)}{\partial d_\circ}$ describes the stability of the damage evolution and $v_{\rm m}(\sigma_\circ) \propto 1/\mathcal{K}(\sigma_\circ)$ is the average dissipation rate. Together, these quantities in the first term of Eq. (10) describe the external loading conditions driving the damage evolution. On approaching failure, damage evolution becomes increasingly unstable, i.e., $\mathcal{K} \rightarrow 0$ and the dissipation rate $v_{\rm m}$ diverges as a power law. The middle term of Eq. (10) describes the non-local effects in the damage field. The last term in the evolution equation (10) describes the disorder in the field of damage resistance.

Interestingly, Eq. (10) is reminiscent of the motion of driven disordered elastic interfaces [45, 46]. This seemingly allows for an interpretation of the precursory damage activity as avalanches during the depinning of an elastic interface (representative of the damage level) that is progressively less stable as it is driven over a disordered field of damage resistance [40, 41]. In the following we show how such an interpretation may not be relevant for failure scenarios where the damage hardening is low and corresponds to a rather short precursory damage accumulation phase.

Damage hardening

We will now seek to characterize the extent of precursory damage accumulation during the failure of brittle disordered solids. From Eq. (11), it follows that stability of the elements during incremental damage can be tuned by considering different hardening levels, i.e., by increasing the material's resistance $Y_{\rm co}$ with increasing damage level $d_\circ$. In the current study, hardening is ensured through the rule, $Y_{\rm co}(d_\circ) = Y_{\rm c}^\circ(1+\eta d_\circ)$ where $Y_{\rm c}^\circ$ is the characteristic damage resistance corresponding to the elastic limit of the equivalent homogeneous medium and η is the hardening coefficient. As a result, the first term of the stability criterion in Eq. (11) is

$$\frac{\partial Y_{\rm co}}{\partial d_\circ} = \eta\, Y_{\rm c}^\circ. \tag{12}$$

While the hardening behavior is at odds with the routine considerations of brittle constitutive response for the elements in earlier studies of brittle solids, it can be directly attributed to the mesoscopic scale description adopted here. The progressive damage evolution of the individual material elements in the current study is representative of expending the distribution of microfracturing thresholds at lower length scales. Such a multiscale interpretation may bridge the discrete failure models such as (global load sharing) fiber-bundle to the damage mechanics framework that considers materials as homogeneous continua [62, 63].

Importantly, damage hardening ensures the progressive degradation at the mesoscopic scale prior to peak load, an observation consistent with the experimental observations [48–54]. The various physical mechanisms observed in experiments that are reminiscent of damage hardening are discussed later in section IV. We note that damage hardening is routinely considered in models of continuum damage mechanics (see *e.g.*, Pham *et al.* [64]) as well as in studies examining the precursors to failure in brittle disordered solids [12, 50, 52, 62, 65–68].

Numerical implementation

To study the effect of damage hardening on the failure behavior of brittle solids, we consider a 2D isotropic elasto-damageable solid under plane stress conditions. Similar to the experiments in Mayya *et al.* [41], the solid of length L, height H and width W is submitted to an external loading F along the vertical axis while being confined laterally. Following Hooke's law, the homogeneous state of stress at the macroscopic scale writes as

$$\boldsymbol{\sigma}_\circ = \sigma_0 \begin{bmatrix} \nu & 0 & 0 \\ 0 & 1 & 0 \\ 0 & 0 & 0 \end{bmatrix} \tag{13}$$

where $\sigma_0 = F/LW$ is the nominal stress imposed by the loading machine. Beyond the elastic limit, the solid undergoes intermittent damage evolution. At the macroscopic scale, it manifests as a progressive degradation of the material's elastic modulus $E_\circ(d_\circ)$, described here as $E_\circ(d_\circ) = E^\circ(1-d_\circ)^2$ with E° being the elastic modulus of the native material. Following Eq. (3), we then obtain the damage driving force of the solid at the macroscopic scale $Y_\circ(d_\circ, \boldsymbol{\sigma}_\circ)$ as $Y_\circ(d_\circ, \boldsymbol{\sigma}_\circ) = -\frac{(1-\nu^2)\sigma_0^2}{2}\left[\frac{E'_\circ(d_\circ)}{E_\circ(d_\circ)^2}\right]$. We note that equilibrium requires $Y_\circ(d_\circ, \boldsymbol{\sigma}_\circ) = Y_{c\circ}(d_\circ)$. Consequently, for the case of homogeneous damage evolution, the levels of stress and strain at the macroscopic scale can be expressed as parametric functions of the average damage level $d_\circ$,

$$\begin{cases} \sigma_0(d_\circ) &= \dfrac{E_\circ(d_\circ)}{\sqrt{1-\nu^2}}\sqrt{\dfrac{-2Y_{c\circ}(d_\circ)}{E'_\circ(d_\circ)}}, \\ \epsilon_0(d_\circ) &= \dfrac{1}{\sqrt{1-\nu^2}}\sqrt{\dfrac{-2Y_{c\circ}(d_\circ)}{E'_\circ(d_\circ)}}. \end{cases} \tag{14}$$

We then determine the interaction kernel $\psi(d_\circ)$ for the boundary conditions being considered using the perturbative approach discussed earlier. In Cartesian coordinates, the interaction kernel writes as

$$\psi(d_\circ) = \left[\frac{E'_\circ(d_\circ)^2}{E_\circ(d_\circ)^3}\right](1-\nu^2)\sigma_0^2\left[\frac{x^4 - 3y^4 + 6x^2y^2}{4\pi(x^2+y^2)^3}\right]. \tag{15}$$

In polar coordinates, the kernel $\psi(r,\theta) \sim g(\theta)/r^2$ implying the elastic interactions are of the long-range type. The anisotropy in energy redistribution during incremental damage is clear in the functional form of the interaction kernel shown in Fig. 1(a). We note that only the adjacent horizontally located regions are reloaded after an elementary damage event.

We model the damage evolution Eq. (10) as a cellular automaton following the protocol presented in Fig. 1(b). Simulations are performed on a square lattice of size $L = 51$ with periodic boundary conditions. Similar boundary conditions are routine in studies on amorphous solids (see *e.g.*, Tyukodi *et al.* [69]). Starting from a heterogeneous field of damage resistance, the stress is increased such that the damage criterion is satisfied at only one of the material elements $\vec{x} = \vec{x}_0$. Following the local damage growth $d(\vec{x}_0, t) = d(\vec{x}_0, t) + \delta d_\circ$ in the damage field $d(\vec{x})$, the local driving force $Y[d(\vec{x}_0,t), \sigma_\circ]$ and the local damage resistance $Y_c[d(\vec{x}_0,t)]$ are updated by $\frac{\partial Y_\circ}{\partial d_\circ}\delta d_\circ$ and $\frac{\partial Y_{c\circ}}{\partial d_\circ}\delta d_\circ(1+\varepsilon)$, respectively. Here ε is a small number drawn from a narrow Gaussian distribution $\mathcal{N}(0, 0.05)$ to preserve the heterogeneous nature of damage resistance field during the successive increments of damage in the material elements. The driving force in remaining elements is also updated as per $\psi(\vec{x} - \vec{x}_0)\delta d_\circ$. Consequently, damage criterion may be now satisfied in one or more elements, setting off a cascade that stops when the redistributions are overcome by material disorder. Again, the stress is increased such that the damage criterion is satisfied at one of the material elements. As a result, damage during the force-control experiment evolves in a bursts-like manner. The total energy dissipated during a typical damage cascade S writes as $S = \sum Y_c(\vec{x}_i, t)\Delta d(x_i)$ where $\Delta d(x_i)$ is the total incremental damage at $\vec{x} = \vec{x}_i$.

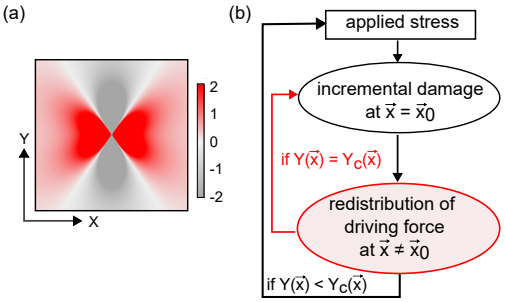

FIG. 1. (a) Functional form of the kernel $\psi(d_\circ)$ for the case of uniaxial compression in 2D. (b) Schematic of the feedback-loop during the damage evolution in brittle disordered solids.

To study the effect of damage hardening on the failure behavior of brittle solids, we consider a constant value of characteristic damage resistance $Y_c^\circ = 1.4$ kJ/m^3 and vary the hardening coefficient η. The elastic constants are as follows - Young's modulus of the initial undamaged material $E^\circ = 1.0$ MPa and the Poisson ratio $\nu = 0.26$. Also, the value of the incremental damage $\delta d_\circ = 0.005$. While these values are similar to the experimental observations of Mayya *et al.* [41] it is verified that the choice of values do not affect the insights of the present study. Lastly, for examining the role of disorder, the heterogeneity in the initial field of damage resistance is defined through a Gaussian distribution of standard deviation β. Table I provides the range of the disorder β and the hardening coefficient η considered in the present study.

TABLE I. The investigated values of disorder and hardening.

material disorder, β	: 0.05, 0.1, 0.15, 0.2, 0.25, 0.3, 0.35, 0.4, 0.45, 0.5
hardening coefficient, η	: 0.05, 0.5, 1, 2.0, 2.5, 3, 5, 10, 15, 25

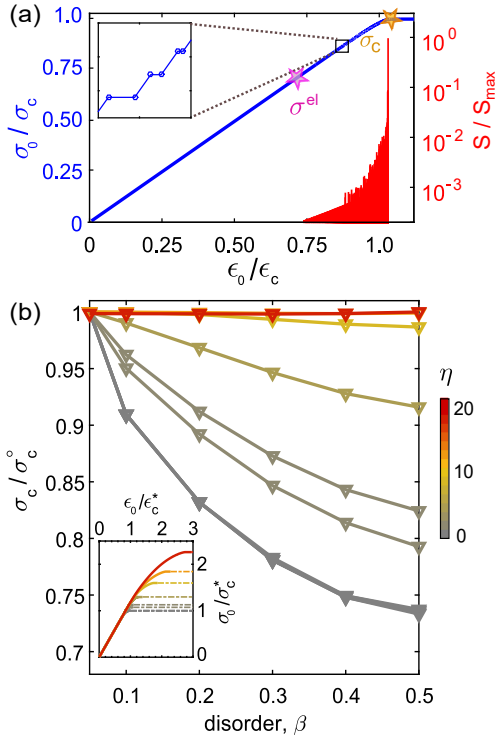

FIG. 2. (a) Typical stress-strain response (in blue) from the damage model obtained for the hardening coefficient $\eta = 2.5$ and disorder $\beta = 0.2$. Inset: Damage cascade manifests at the macroscopic scale as a stress plateau. The size of precursory damage cascade S normalized by the maximum value $S/S_{\max}$ (in red) is shown to increase on approaching failure. (b) Variation of the normalized critical stress σ_c/σ_c° with the strength of disorder β for different values of the hardening coefficient η. Here σ_c° is the value for the case of disorder $\beta = 0.05$. Inset: Effect of damage hardening on the stress-strain response for a fixed disorder $\beta = 0.2$. σ_c^* and ϵ_c^* are the values of stress and strain at the onset of failure for the case $\eta = 0.05$.

III. RESULTS

The typical stress-strain response (in blue) obtained from the simulations with moderate disorder and low hardening is shown in Fig. 2(a). Beyond the elastic limit σ_{el}, we find the macroscopic response is a sequence of stress plateaus and elastic loading segments (see inset of Fig. 2(a)). The stress plateaus correspond to dissipative bursts of mechanical energy as shown in Fig. 2(a) (in red). At the local level, a cascade of micro-instabilities in the damage field are progressively stabilized by either disorder or by the unloading during the elastic energy redistributions. However, at the critical value of stress σ_c, the damage evolution in the force-control experiment becomes unstable resulting in a catastrophic failure.

To decipher the role of the damage hardening η, we first examine the failure stress σ_c. For a fixed value of disorder β, increasing the damage hardening manifests a higher value of critical stress σ_c as well as critical strain ϵ_c, see inset of Fig. 2(b) (also Appendix A). This is consistent with the increased ductility at the local scale. However, when the damage hardening η is fixed, the role of disorder is not straightforward. We find that the specimen strength σ_c decreases with the increasing strength of disorder β especially when the hardening η is small, as shown in Fig. 2(b). For large hardening, however, the strength σ_c is nearly independent of the disorder. Notably, this is at odds with earlier studies that considered brittle constitutive response at the local scale [30–33]. The non-trivial effect raises new questions on the connection between the damage hardening and the nature of failure. Contrary to the central role of the disorder in the critical point interpretation of failure, here we find that the role of disorder is diminished as damage hardening is increased. The nature of failure may indeed vary with damage hardening. It then follows that such a transition will also reflect in the scaling description of failure precursors.

A. Criticality during the approach to failure

We will now examine the statistics of precursors for the different scenarios described in Fig. 2(b). In the right-hand side axis of Fig. 2(a), we find that the precursor size S increases close to failure. To contextualize their evolution, we define the distance to failure $\delta = (\sigma_c - \sigma_0)/(\sigma_c - \sigma_{el})$ and measure the variation of the dissipation rate dE_d/dt with δ. As $dE_d/dt \sim \langle S \rangle$, the average size of the precursors [41], we find the energy dissipation to increase as a power law with the distance to failure $dE_d/dt \propto \delta^{-\alpha}$ for nearly all values of disorder and hardening. The value of the exponent α is, however, not a constant.

From the exponent α for different values of disorder and hardening coefficient, we obtain a phase diagram providing the material quasi-brittleness as a function of β and η, see Fig. 3. The bottom left corner of this diagram and its vicinity correspond to weak disorder and low hardening, and describe brittle failure (in black). Here the precursory activity is scarce and we did not

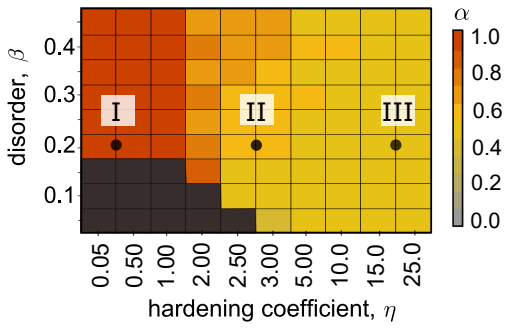

FIG. 3. Values of the exponent α characterizing the power law divergence of dissipation rate on approaching failure for different values of disorder β and hardening coefficient η. We note the bins on the abscissa to be non-uniform.

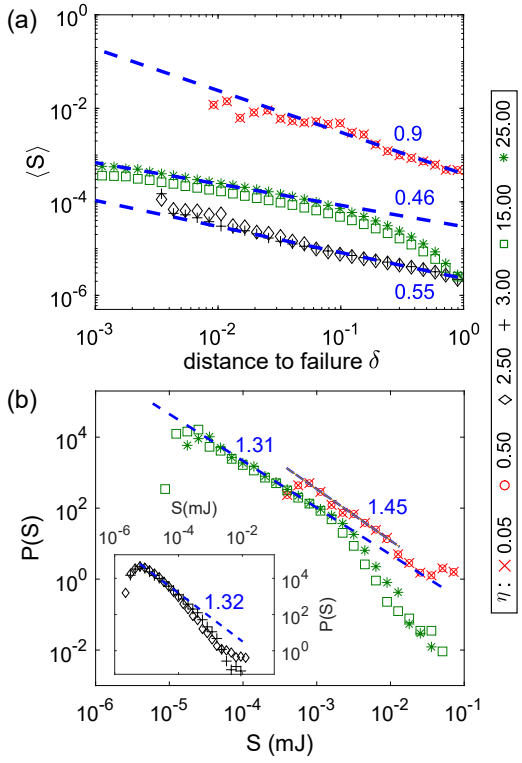

FIG. 4. (a) Divergence of the average precursor size $\langle S \rangle$ with the distance to failure δ. (b) Distribution of the precursor sizes S from the data obtained close to failure $\delta \to 0$ for regimes I and III (main panel) and regime II (inset).

characterize their statistics. Increasing the strength of disorder, we obtain a quasi-brittle failure behavior, an observation that is in good agreement with *toy models* provided in the literature [30–32]. Here, the value of the exponent $\alpha \simeq 0.9$. Next, for the case of moderate hardening, we obtain a smaller value of exponent α. Notably, even when the disorder is weak, we find $\alpha \simeq 0.5$ (see *e.g.* $\beta \simeq 0.05, \eta \simeq 5.0$). Similarly when the hardening is large, the value of exponent $\alpha \simeq 0.5$. To explain these behaviors, we now analyze in detail, the representative cases of each regime. In Fig. 3, we consider regimes I and III as typical of the damage spreading when hardening is small and large, respectively and nominally consider the transition as regime II. We take two sets of data for each regime $\eta = \{0.05, 0.5\}; \{2.5, 3.0\}; \{15, 25\}$ at a fixed disorder strength $\beta = 0.2$.

The divergence of the average precursor size $\langle S \rangle$ with the distance to failure δ is shown in Fig. 4(a) for each case. The scaling exponent $\alpha = 0.9 \pm 0.04$ for regime I, $\alpha = 0.55 \pm 0.02$ for zone II and $\alpha = 0.46 \pm 0.01$ for zone III. Beyond different exponents, we find the smallest value of δ reached at failure is different from one regime to another. The rather prolonged precursory phase goes along with a smaller exponent and highly intermittent damage evolution. Moreover, at a fixed distance to failure, the precursors in regime I are typically larger than the precursors in regimes II and III.

We then compute the distribution of precursor sizes S close to failure ($\delta \to 0$) and obtain a power law $P(S) \propto S^{-\tau}$ for all data-sets as shown in Fig. 4(b). The exponent in regimes II and III was $\tau = 1.31 \pm 0.05$ and $\tau = 1.32 \pm 0.1$, respectively. For precursors from regime I, a higher value $\tau = 1.45 \pm 0.05$ is obtained.

The scale-free statistics of precursors and their divergence as failure is approached seemingly argue for a critical phenomenon interpretation [6–13, 42]. In Mayya *et al.* [41], we untangled these same features during compressive failure by showing that precursors as avalanches reminiscent of the depinning of a non-standard disordered elastic interface [45, 46]. Failure, on the other hand, was shown to correspond to the onset of localization, a standard instability in the homogeneous damage evolution. The power law divergence of the dissipation rate in this case was then obtained by a linearization of the damage evolution equation (1) providing a theoretical prediction for the exponent $\alpha = 1/2$ [40, 41].

As the values of damage hardening $\eta = \{15, 25\}$ in regime III are comparable to the one measured in the experiments of Mayya *et al.* [41] ($\eta \simeq 45$), we interpret the precursors obtained for large damage hardening as depinning avalanches. Also, the value of $\alpha \simeq 0.46$ matches rather well with the theoretical prediction. In Mayya *et al.* [41], the stress at failure σ_c derived using the assumptions of homogeneous damage evolution considerations was nearly independent of the strength of disorder, a prediction that is in rather good agreement with the variations of σ_c with disorder β for regime III, see Fig. 2(b). For the case of moderate hardening, we also find $\alpha \simeq 0.5$ (see Fig. 4(a)). But there is a slight variation in the failure stress with disorder. However, precursors in regime I provide an exponent $\alpha \simeq 0.9$, a significantly larger value.

B. Criticality of precursors for low hardening

To explain the different behavior of precursors in regime I, we examine the elements undergoing incremental damage. As shown in Fig. 5(a), the element selected as the seed, i.e., the first damaged element in a cascade is affected by hardening. We find the damage resistance of the seed Y_c^{seed} to be constantly lower than the average value $Y_c^{\text{seed}} < \langle Y_c \rangle_x$. This is at odds with the behavior observed in case of regimes II and III for which beyond a transient stage, the damage resistance of the seeds is comparable to the average value $Y_c^{\text{seed}} \sim \langle Y_c \rangle_x$. This last behavior suggests the participation of all elements during the damage spreading process. In contrast, for regime I, only weaker elements of the damage resistance field participate in avalanches, even very close to failure. Clearly, the damage fields of these regimes merit a closer look and will be discussed later in section III C.

We now focus on the incremental damage evolution of the elements. The variation of the average incremental damage Δd^* computed per element during a cascade as a

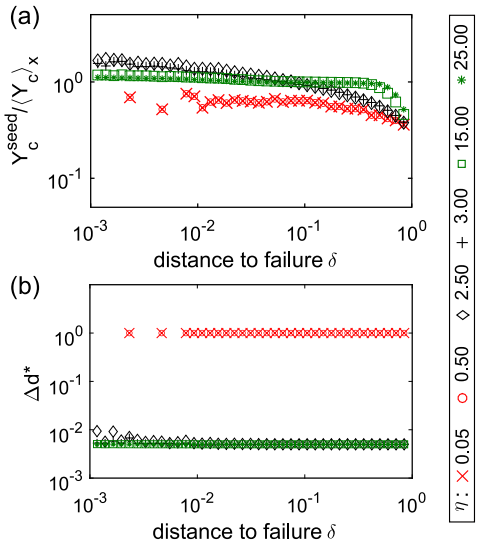

FIG. 5. Variation of (a) the damage resistance of the avalanche seed Y_c^{seed} normalized by the average value $\langle Y_c \rangle_x$ and (b) the average incremental damage Δd^* in the activated elements during the cascade with the distance to failure δ.

function of the distance to failure, δ is shown in Fig. 5(b). The material elements during regime I fail completely ($\Delta d^* = 1.0$). As a result, on approaching failure, the concentration of failed elements p increases rapidly close to failure, see inset of Fig. 6(a). In contrast, the material elements for regimes II and III participate only once during damage cascades as $\Delta d^* = \delta d_\circ$, the incremental damage taken to be 0.005 in the present study, as shown in Fig. 6(a). The concentration of failed elements p is therefore (nearly) zero during most of the damage accumulation when damage hardening is (moderately) large.

These disparities in the damage evolution further argue for a different universality class for damage spreading of regime I. In particular, the strong influence of disorder, the participation of weaker elements and an increasing concentration of the failed elements on approaching failure are in violation with the framework describing failure as the depinning of a non-stationary disordered elastic interface [41]. These aspects are rather reminiscent of the percolation type damage spreading observed in discrete models [23, 28, 30–32, 37, 70]. In these studies, as driving is increased, numerous clusters of failed elements nucleate and merge with existing ones; Their size increases until failure that corresponds to a system-spanning cluster rupturing the remaining backbone.

We examine this idea further through the distribution of cluster sizes s_c in the damage field obtained prior to failure, see inset of Fig. 6(b). This presents yet another scaling relation $P(s_c) \sim s_c^{-\tau_c}$ with $\tau_c = 2.18 \pm 0.1$. Notably, this exponent is in rather good agreement with the predicted value 2.05 at the percolation threshold in 2D [30]. We find that the scaling is independent of the specimen size $L \in [101, 151, 201]$. Interestingly, in Fig. 6(b), the size of the largest cluster is found to increase with specimen size suggesting finite-size effects. The exponent $\alpha \simeq 0.9$ in regime I is also in rather good agreement with the value $\alpha \simeq 0.86$ reported in case of a 2D fiber bundle model with global load sharing [37, 70]. Strikingly, these results provide a critical point description of failure instead of an instability [40, 41]. Estimating the strength σ_c is then not straightforward.

The difference in the nature of failure is also clear from the damage field. Contrary to regime III, at the onset of failure, the damage field in regime I is strongly heterogeneous, see top panel of Fig. 7. Larger the hardening, more homogeneous the damage evolution. Interestingly, all regimes display a thin band within which the damage concentrates at the onset of failure. The overlap in the profiles of the macroscopic fault for regimes I and II is significant. It highlights the strong role of disorder during damage evolution for these regimes [29]. However, the localization of damage taking place in regime III is distinctly different, further arguing for a different interpretation of failure for large hardening.

Outside the localization band, the damage field contains the signature of the precursors. On the one hand, in regime I, we observe numerous clusters that are nearly linear highlighting the role of the interaction kernel $\psi(\sigma_\circ)$ that prescribes reloading of the driving force along the horizontal axis. For regime II, we find a similar damage field. However, the damage level in the elements for this case is rather distributed. On the contrary, the damage field outside the localization band in regime III appears

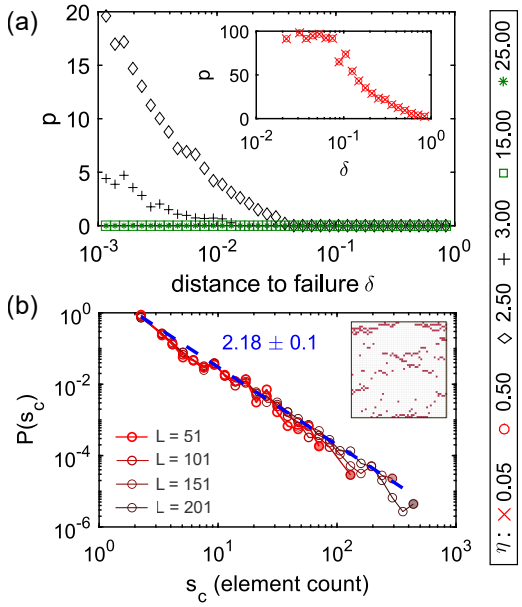

FIG. 6. (a) Variation of the concentration of failed elements p with the distance to failure δ. Inset: Data for regime I. (b) Distribution of the size of the clusters s_c in the damage field when the damage hardening is low ($\eta = 0.5$) and the disorder is moderate ($\beta = 0.2$) for varying specimen size L. The largest clusters in each case are marked as solid circles. Inset: Damage field before failure in a typical specimen.

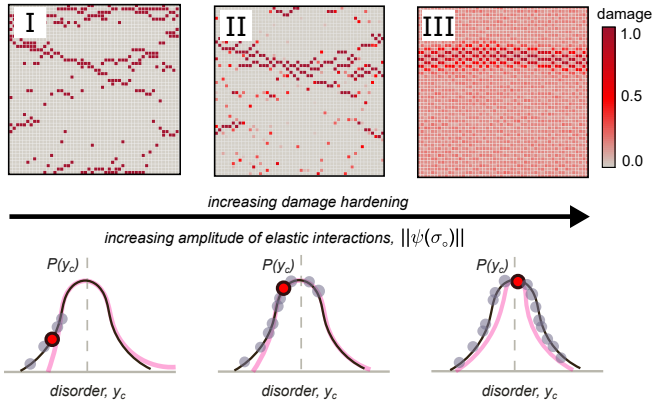

FIG. 7. Top : Typical damage field at the onset of failure for regimes I ($\eta = 0.5$), II ($\eta = 2.5$) and III ($\eta = 25$) depicting the transition from a heterogeneous to a homogeneous damage evolution. It denotes various versions of damage spreading that are dominated by material disorder and elastic interactions, respectively. Bottom: The schematic showing the activity on the distribution of disorder y_c during one damage cascade for different cases of hardening. Cascade begins with the damage evolution at the seed (red dot). We note the position of the seed for regime III could be anywhere along the distribution. The redistributions that follow may satisfy the damage criterion for other elements belonging to different regions (gray dots) of the distribution. Consequently, the original Gaussian distribution of the disorder (in black) may be transformed on approaching failure to the one shown in magenta, see also Appendix B.

to be nearly homogeneous. As the strength of disorder at the beginning of the damage accumulation in all three cases was fixed ($\beta = 0.2$), these observations argue for a connection between hardening and elastic interactions.

C. Effect on the damage feedback-loop

We now interpret the effect of damage hardening through the competition between disorder and elastic interactions [34, 39]. Using the original distribution $P(y_c)$ in the damage resistance as a reference (black curve), we track the events during a typical damage cascade as shown in the bottom panel of Fig. 7. Hardening is shown to control the range of the disorder distribution that is activated (gray dots), following the seed (red dot).

When the damage hardening is low, the damaged elements fail completely. The resulting redistribution of energy is only sufficient to trigger damage growth in the weaker elements located on the left-hand side of the distribution. The weaker elements are thus progressively expended and close to failure, the distribution has a leaner left-branch (curve in magenta). For the case of large hardening in regime III, the elements that are active during the cascade are stabilized immediately resulting in a rather small increase in their damage level. As a result, the elements interact with each other more frequently and reshape the whole disorder distribution (i.e., the whole damage field) as failure is approached (curve in magenta). Another consequence of large hardening is the delayed onset of failure. This allows for a larger amplitude of the elastic interactions $||\psi(\boldsymbol{\sigma}_\circ)||$ as hardening is increased. Therefore, even though the elements undergo a small incremental damage, the redistributions are large. During damage evolution, even the stronger elements are activated, resulting in a rather homogeneous damage evolution.

As a result, by increasing the hardening, we shift from disorder dominated to an elastic interactions dominated damage spreading mode. At intermediate levels, damage mostly explores the weaker elements of the distribution but in contrast to regime I, the damage growth is stable. In support to this interpretation, we track the distribution $P(y_c)$ with different distances to failure. We obtain a leaner left-branch in regime I and a Gaussian distribution in regime III, close to failure (see Appendix B).

D. Quasi-brittleness phase diagram

Finally, we show in Fig. 8, a 2D parametric space depicting the effect of disorder (abscissa) and hardening coefficient (ordinate). Close to the origin where disorder is weak ($\beta \to 0$) and damage hardening is low ($\eta \to 0$), failure is brittle. The right-hand side of the diagram corresponds to the case of a rather homogeneous damage evolution (regime III). Here, the intermittent damage evolution is reminiscent of the avalanches during the

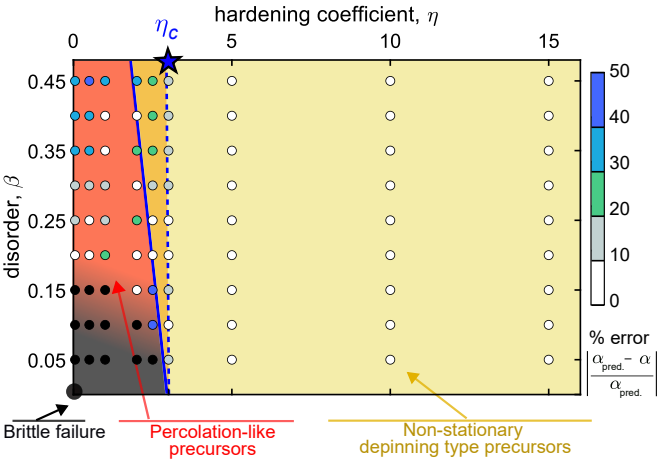

FIG. 8. Phase diagram depicting the different regimes of intermittent damage evolution during quasi-brittle failure - percolation (red) and non-stationary depinning (yellow). The narrow transition regime (orange) is bounded by the theoretical prediction Eq. (16) (blue line) and the threshold for homogeneous damage evolution (dashed line). The approach to failure in these regimes is understood to provide the scaling exponent $\alpha_{\text{pred}} \simeq 0.9$ and $\alpha_{\text{pred}} \simeq 0.5$, respectively. The deviation of the exponent α obtained for different values of disorder β and hardening η from the theoretical prediction is also shown (marker color).

depinning of a driven disordered elastic interface. The characteristic features of the precursors including their size, length scale and timescale are related to each other by scaling relations with critical exponents [40, 41]. On the left-hand side, at moderate disorder, i.e., regime I, we expect a percolation type criticality for the precursors. Here unlike regime III, the characteristics of the cumulative damage field are described by critical exponents emerging from percolation. Following Figs. 3, 4 and 7, we expect a cross-over regime II where the damage spreading resembles both regimes I and III. While a distinct transition from nucleation (brittle) to percolation is also proposed at the cross-over in disorder strength in a recent phenomenological model set at the thermodynamic limit [35], such a boundary was ambiguous in the present study involving finite sized specimens. Therefore, we did not include it in the quasi-brittleness diagram.

To obtain the bounds of the different damage spreading modes, we revisit regime I. As the elements undergo unstable damage, we seek to find the threshold value $\eta_{\rm th}$ for hardening when damage is stable. The average resistance of the damaged elements in this case, i.e., the left-branch of $P(y_{\rm c})$, is given by $Y_{\rm c\circ} = Y_{\rm c}^{\circ}(1-\beta\sqrt{2/\pi})$, see Appendix C. Here $\beta\sqrt{2/\pi}$ is the mean value of the half-normal distribution describing the elements on the left branch of the disorder distribution. From the stability criterion and by considering an infinitesimal increase in damage level ($d_\circ \to 0$), we obtain

$$\eta_{\rm th} \simeq 3(1-\beta\sqrt{2/\pi}). \tag{16}$$

The solution of the above equation is represented by the blue line in Fig. 8. It marks the upper bound for the unstable damage spreading mode (regime I). Setting $\beta = 0$ in Eq. (16) would imply disregarding the effect of disorder in the stability criterion. This is reminiscent of the damage spreading in regime III. We thus obtain $\eta_{\rm c} \simeq 3$ as the lower bound for homogeneous damage evolution (and depinning type avalanches). These predictions match rather well with the numerical results of Fig. 3. For validating the proposed scenario, the deviations $|1-\alpha/\alpha_{\rm pred.}|$ from the predicted value $\alpha_{\rm pred.}$ are also plotted in Fig. 8 (solid circles) with $\alpha_{\rm pred.} = 0.9$ for regime I and $\alpha_{\rm pred.} = 0.5$ for regime III. We find a difference between the measured exponents and the predicted one to be less than 20%, especially at moderate disorder.

IV. DISCUSSION AND CONCLUSION

Before taking up the implications of our findings, we would like to discuss the origins of damage hardening that has been described here using a continuum mechanics approach by the hardening coefficient η. The progressive damageability at the mesoscopic scale may be attributed to both loading conditions as well as microstructural aspects. For example, during compressive failure, the activation of defects such as microcracks, porosity, etc. due to stress concentration is countered by the remotely applied stress [48–54]. As a result, on increasing the driving, the material may still resist the local loading but then displays lower stiffness. The density of microcracks therefore continues to increase until failure at which macroscopic load bearing capacity decreases owing to damage localization [1–3, 55]. On the contrary, failure under traction may result from the catastrophic growth of damage from one of the defects resulting in a relatively short damage accumulation phase.

The presence of confinement or temperature may also influence the damage hardening behavior by altering the nature of microcracking processes : From tensile to shear cracks in crystalline rocks [71, 72], from dilatant failure to compaction shear banding in porous rocks [73] and from microcracking to plasticity in silicate rocks [74]. In porous rocks, when the intricate structure of porosity and flaws was varied, a variation in both the precursors as well as final failure is observed [75, 76]. Also, prolonged damage accumulation in complex materials is attributed to the hierarchical organization of material [22, 77, 78]. Thus, hardening can be considered as a key feature of a mesoscopic scale description of damage evolution in brittle solids. As we will discuss in the following, its influence on precursors' statistics as well as load bearing capacity have important implications for quasi-brittle failure.

The exponent α describing the divergence of precursors close to failure is an important signature of the hardening. Interestingly, this provides an explanation of the large scatter in the acoustic activity data reported in literature. To connect the acoustic emissions with damage cascades, we use the empirical relation $\alpha_{N_{\rm AE}} \simeq 1.3\,\alpha$ recently reported in the literature [41, 47]. This relation is consistent with our theoretical understanding of acoustic emissions: Damage cascades are composed of several highly correlated clusters and each of them may lead to individual acoustic hits. Therefore, the waiting times between successive damage cascades are exponentially distributed as expected for a Poissonian process whereas the waiting times between acoustic events routinely display a power law [10]. Therefore, the value of the activity rate exponent $\alpha_{N_{\rm AE}}$ is different from α.

Here, using the relation $\alpha_{N_{\rm AE}} \simeq 1.3\,\alpha$ to translate the value of α measured in our simulations to $\alpha_{N_{\rm AE}}$, we can compare the different acoustic measurements reported in literature. Close to the lower bound $\alpha_{N_{\rm AE}} \sim 0.5-0.8$ corresponding to $\alpha \sim 0.4-0.6$, we expect the damage spreading to entail large hardening. On the other hand, $\alpha_{N_{\rm AE}} \geq 1.2$ corresponding to $\alpha \geq 0.9$ points at low hardening. $\alpha_{N_{\rm AE}} \sim 1.0$, then corresponds to a transitional case where effects of both hardening and strength of disorder are at play.

The exponent characterizing the distribution of avalanche sizes τ may also be used to qualitatively infer the spatial correlation in the damage field. Homogeneous damage spreading has been shown to present a smaller value of τ [29], similar to our findings for the case of large hardening. Consequently, we infer that a

smaller value of τ_{AE}, the counterpart in terms of acoustic emissions may be used to infer a relatively higher hardening behavior especially between specimens with similar preparation methods [8, 78]. This understanding is also consistent with acoustic experiments of compressive failure of Sidorbe granite under confinement [52]. Interestingly, our interpretation allows for insights on the meso-scale damage accumulation in complex materials such as bone, charcoal, etc. Smaller values of τ_{AE} were reported in case of remodeled microstructural samples of porcine and bovine cortical bone under compression [22, 77]. The implied increase of damage hardening is consistent with the notion that bone remodeling leads to improved properties at lower length scales. Similarly, the exponents during compressive failure of homogeneous samples of charcoal with micro- and nano-pores were reported to be smaller than the value obtained for samples with macroscopic voids and heterogeneities [79]. Nevertheless, a definitive inference of quasi-brittleness from the exponent τ_{AE} may require further study. Contrary to the scatter reported for $\alpha_{N_{\mathrm{AE}}}$, the range of the exponent τ_{AE} is narrow. Also in some materials, the mixing of signals from different sources may distort the inference on hardening [17, 80, 81].

The relevance of damage hardening pertains to yet another important aspect of our results - the predictability of the failure load of materials. With increasing utility of precursors in failure prediction, precise exponents based on hardening may be provided for the algorithms using numerous time-to-failure scaling laws in their monitoring systems. From an engineering perspective, it is useful to reinforce structures such that damage hardening is sufficiently large. Strategies such as confinement at the boundaries, heat treatment, etc., for example may be employed. This not only ensures the stress at failure is less sensitive to the strength of disorder at the mesoscopic scale but also facilitates an early anticipation of failure from the analysis of the larger population of precursors.

Another subtle but an important advantage of damage hardening concerns the finite-size effect. When hardening is low, the strength varies with both specimen size as well disorder [24, 31, 33]. This makes the estimation of strength in large specimens difficult as heterogeneity levels may vary with specimen size. In addition, owing to the brittle constitutive response, nucleation-type failure is anticipated at the thermodynamic limit [24, 30]. However, an enhancement to moderate hardening diminishes the influence of disorder. Failure of larger specimens is then preceded by an increased number of precursors. As a result, the effect of elastic redistributions increases manifold and the initial disorder distribution of the damage field is reshaped to a greater extent. Consequently, larger specimens may present a smaller variability of strength. A size-effect is revealed for both strength and the inter-specimen variability in this case [13, 42]. For large hardening, the damage evolution is homogeneous, even for finite-sized specimens. The size-effect on strength for this case may therefore be minimal. A detailed examination of the finite-size effects in relation to hardening is left as future studies.

Finally, we note the limited significance attributed to the strength of disorder in the current study is still consistent with the results from earlier models of quasi-brittle failure. For small hardening, we find the damage evolves through the weakest elements and that the strength of disorder controls the extent of damage accumulation - from nucleation to percolation [30, 31, 35]. Strikingly, this is but a partial picture. We find that there is an additional regime where damage evolution may be implicitly dominated by the long-range elastic interactions. As a result, a diffused damage field can be realized even for weak disorder, an observation that is in good agreement with studies that explicitly tune the range of elastic interactions between the materials elements [34, 37, 39]. Importantly, our mesoscopic scale representation of the co-operativity between disorder and elastic interactions is consistent with experimental observations of scale-free statistics during the compressive failure of weakly disordered solids [16].

In summary, here we show that hardening has an integral role in the co-operative dynamics of damage growth emerging from the interplay of disorder and elastic interactions. It not only drives the extent of precursory damage accumulation but also affects the statistics of the precursors. Indeed, the linear hardening behavior considered here may be deemed rather simple. Moreover, the interaction kernel is derived using homogeneous damage evolution considerations. Such considerations may not capture the finer aspects of the damage spreading in complex materials, especially for the case of low hardening. Discrete models where interactions are implicitly defined may be better suited for the low hardening case. Also, the use of periodic boundary conditions instead of ordinary boundary conditions may carry limitations on the insights during the onset of damage localization [82]. Still, our findings bring out the rich physics emerging from damage hardening and reconcile the existence of two universality classes of criticality discussed till date in relation to quasi-brittle failure. On one hand, the interpretation of percolation is retrieved for low hardening, similar to the discrete models such as random fuse/spring, fiber bundle, etc. On the other hand, the depinning type scaling description of precursors is disentangled from the approach of localization during compressive failure, i.e., large hardening. This conveys distinctly different interpretations for the nature of failure - a critical point and a standard instability, respectively. The signature of approaching failure is also different. The exponent is much larger for percolation. Our findings thus help unravel the connection between the level of quasi-brittleness and precursor statistics. Also, the wide-scatter in the values of the scaling exponents reported in literature can be rationalized. These insights pave the way for quantitative inferences about quasi-brittleness of materials in real-time, a topic of strategic interest during the damage monitoring of mechanical parts and structures.

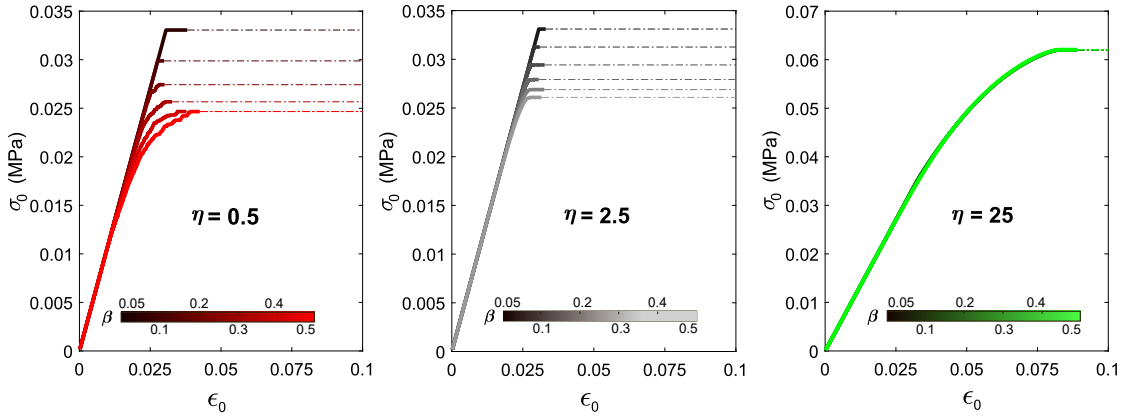

FIG. 9. The typical stress-strain response obtained for a given hardening coefficient and varying strength of disorder in each panel. Stronger disorder is shown in brighter colors. The damage hardening of the data-sets increases from left to right.

ACKNOWLEDGMENTS

We thank Laurent Ponson for the insightful discussions on the finer aspects of the non-local damage model. Also, we thank Anne Tanguy, member of the editorial board and other reviewers for their feedback on the manuscript. We gratefully acknowledge the financial support from Sorbonne Université, Centre National de la Recherche Scientifique (CNRS) and Satt-Lutech through the project, *Development of a technology of predictive maintenance for materials and structures under compression* and from the Centre National d'Études Spatiales (CNES) for the project, *From diagnostic to prognostic in structural health monitoring.*

Appendix A: Individual roles of disorder and damage hardening

The macroscopic response obtained for a fixed hardening coefficient and varying disorder is shown in different panels of Fig. 9. We note the material disorder β plays an important role when damage hardening is low. Failure is shown to occur at progressively lower value of stress and a higher value of failure strain. The transformation in damage spreading is evident on increasing the hardening coefficient η (panels from left to right). For large hardening, the value of critical stress and strain are found to be independent of the strength of disorder. On the other hand, at fixed disorder, the damage hardening results in an enhanced load bearing capacity.

Appendix B: Evolution of disorder in the damage resistance

We track the distribution of the damage resistance with distance to failure to decipher the changes in disorder with damage hardening. As shown in Fig.10 when hardening is low, the left branch of the distribution becomes progressively leaner. Only the weaker elements are expended during damage spreading. As the incremental damage in this case is large, see Fig. 5(b), the changes to the local damage resistance is very large. Consequently, these elements appear distinctly on the right branch of the distribution. Similar features are observed when the hardening is moderate. However, the partial damage of the weaker elements results in a nominal increase of the damage resistance and therefore, a second peak on the right branch is absent. We also note that the original right branch is recovered in both cases implying that the strong elements of the distribution did not participate in the damage spreading. In contrast for large hardening, the distribution becomes leaner approaching the Gaussian $\mathcal{N}(Y_{\rm co}, 0.05)$ from the original disordered field, $\mathcal{N}(Y_{\rm co}, 0.2)$. The narrow distribution close to failure rather corresponds to the hardening $\eta Y_{\rm c}^{\circ}\delta d_{\circ}$ being drawn from a narrow Gaussian distribution with standard deviation of 0.05.

Appendix C: Threshold value of hardening for stable damage evolution

As the strength and manner of damage spreading vary with hardening, we expect a threshold value for hardening $\eta_{\rm th}$ at which the elastic interactions prevail over material disorder during intermittent damage evolution. Taking inspiration from the panels on the right-side in Figs. 9 and 10, we first consider the case of homogeneous damage evolution. The stability criterion of the damage evolution following Eq.(11) writes as

$$\mathcal{K} = \frac{\partial(Y_{\rm co} - Y_{\circ})}{\partial d_{\circ}} \geq 0, \tag{C1}$$

where we have also considered the limiting case $\mathcal{K} = 0$. Here, the second term writes as

$$\frac{\partial Y_{\circ}}{\partial d_{\circ}} = \frac{(1-\nu^2)\sigma_0^2}{2}\frac{d}{dd_{\circ}}\left(\frac{-E'_{\circ}}{E_{\circ}^2}\right) \rightarrow \frac{3(1-\nu^2)\sigma_0^2}{E^{\circ}(1-d_{\circ})^4}, \tag{C2}$$

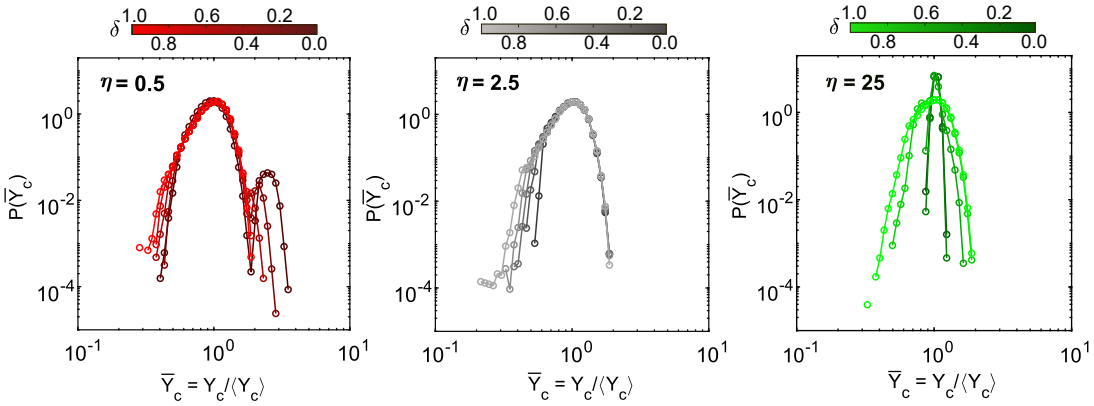

FIG. 10. Distribution of the damage resistance normalized by the mean value $\overline{Y_c} = Y_c/\langle Y_c\rangle$ at fixed damage hardening at different distances to failure δ. The damage hardening of the data increases from left to right.

where $E'_\circ(d_\circ) = -2E^\circ(1-d_\circ)$. From the equilibrium condition $Y_\circ(d_\circ) = Y_{c\circ}(d_\circ)$, we have $\sigma_0^2 = \frac{Y_{c\circ}E^\circ(1-d_\circ)^3}{(1-\nu^2)}$. As a result, we obtain the following.

$$\frac{\partial Y_\circ}{\partial d_\circ} = \frac{3Y_c^\circ(1+\eta d_\circ)}{(1-d_\circ)}. \tag{C3}$$

The terms of the stability criterion given in Eq. (C1) can be then rearranged as

$$\eta \geq \frac{3(1+\eta d_\circ)}{(1-d_\circ)}. \tag{C4}$$

For the incremental damage to be stable, we take $d_\circ \to \delta d_\circ \sim 0$ and obtain the threshold value $\eta_c \simeq 3$ for stable homogeneous damage evolution. When $\eta < \eta_c$, the damage spreading is dominated by the strength of the material disorder β. Close to η_c, one then expects a transition where the incremental damage of the elements is stable. The equilibrium in this case is satisfied by the energy balance of the weaker elements whose average value $Y_\circ(d_\circ) = Y_{c\circ}(1-\beta\sqrt{2/\pi})$. Here, following Figs. 7 and 10, we consider only the left-branch of the original normal distribution. Therefore, for $\eta < \eta_c$ when disorder and elastic interactions are at play, Eq. (C3) writes as

$$\frac{\partial Y_\circ}{\partial d_\circ} = \frac{3Y_c^\circ(1+\eta d_\circ)}{(1-d_\circ)}(1-\beta\sqrt{2/\pi}). \tag{C5}$$

The hardening coefficient η to ensure stable damage growth then writes as

$$\eta \geq \frac{3(1-\beta\sqrt{2/\pi})}{1-d_\circ[1+3(1-\beta\sqrt{2/\pi})]}. \tag{C6}$$

Again by considering $d_\circ \to \delta d_\circ \simeq 0$, we obtain the threshold value $\eta_{\rm th}$ of damage hardening as

$$\eta_{\rm th} \simeq 3(1-\beta\sqrt{2/\pi}). \tag{C7}$$

[1] M. Kachanov, Elastic solids with many cracks: a simple method of analysis, International Journal of Solids and Structures **23**, 23 (1987).

[2] Z. P. Bažant, Nonlocal damage theory based on micromechanics of crack interactions, Journal of engineering mechanics **120**, 593 (1994).

[3] M. J. Alava, P. K. Nukala, and S. Zapperi, Statistical models of fracture, Advances in Physics **55**, 349 (2006).

[4] D. Lockner, J. Byerlee, V. Kuksenko, A. Ponomarev, and A. Sidorin, Quasi-static fault growth and shear fracture energy in granite, Nature **350**, 39 (1991).

[5] J. Fortin, S. Stanchits, G. Dresen, and Y. Guéguen, Acoustic emission and velocities associated with the formation of compaction bands in sandstone, Journal of Geophysical Research: Solid Earth **111** (2006).

[6] A. Petri, G. Paparo, A. Vespignani, A. Alippi, and M. Costantini, Experimental evidence for critical dynamics in microfracturing processes, Physical Review Letters **73**, 3423 (1994).

[7] A. Garcimartin, A. Guarino, L. Bellon, and S. Ciliberto, Statistical properties of fracture precursors, Physical Review Letters **79**, 3202 (1997).

[8] S. Deschanel, L. Vanel, N. Godin, G. Vigier, and S. Ciliberto, Experimental study of crackling noise: conditions on power law scaling correlated with fracture precursors, Journal of Statistical Mechanics: Theory and Experiment **2009**, P01018 (2009).

[9] J. Davidsen, S. Stanchits, and G. Dresen, Scaling and universality in rock fracture, Physical review letters **98**, 125502 (2007).

[10] J. Baró, Á. Corral, X. Illa, A. Planes, E. K. Salje, W. Schranz, D. E. Soto-Parra, and E. Vives, Statistical similarity between the compression of a porous material and earthquakes, Physical review letters **110**, 088702

(2013).
[11] J. Rosti, J. Koivisto, and M. J. Alava, Statistics of acoustic emission in paper fracture: precursors and criticality, Journal of Statistical Mechanics: Theory and Experiment **2010**, P02016 (2010).
[12] L. Girard, D. Amitrano, and J. Weiss, Failure as a critical phenomenon in a progressive damage model, Journal of Statistical Mechanics: Theory and Experiment **2010**, P01013 (2010).
[13] C.-C. Vu, D. Amitrano, O. Plé, and J. Weiss, Compressive failure as a critical transition: Experimental evidence and mapping onto the universality class of depinning, Phys. Rev. Lett. **122**, 015502 (2019).
[14] J. Baró, K. A. Dahmen, J. Davidsen, A. Planes, P. O. Castillo, G. F. Nataf, E. K. Salje, and E. Vives, Experimental evidence of accelerated seismic release without critical failure in acoustic emissions of compressed nanoporous materials, Physical review letters **120**, 245501 (2018).
[15] J. Baró, A. Planes, E. K. Salje, and E. Vives, Fracking and labquakes, Philosophical Magazine **96**, 3686 (2016).
[16] G. F. Nataf, P. O. Castillo-Villa, J. Baró, X. Illa, E. Vives, A. Planes, and E. K. Salje, Avalanches in compressed porous si o2-based materials, Physical Review E **90**, 022405 (2014).
[17] J. Davidsen, T. Goebel, G. Kwiatek, S. Stanchits, J. Baró, and G. Dresen, What controls the presence and characteristics of aftershocks in rock fracture in the lab?, Journal of Geophysical Research: Solid Earth **126**, e2021JB022539 (2021).
[18] L. Wang, S. Cao, X. Jiang, and E. K. Salje, Cracking of human teeth: An avalanche and acoustic emission study, Journal of the Mechanical Behavior of Biomedical Materials **122**, 104666 (2021).
[19] S.-T. Tsai, L.-M. Wang, P. Huang, Z. Yang, C.-D. Chang, and T.-M. Hong, Acoustic emission from breaking a bamboo chopstick, Physical Review Letters **116**, 035501 (2016).
[20] D. Triantis and S. K. Kourkoulis, An alternative approach for representing the data provided by the acoustic emission technique, Rock Mechanics and Rock Engineering **51**, 2433 (2018).
[21] We consider Omori law, the scaling relation associated with the activity rate of events between two successive large signals to also describe the approach to failure [10].
[22] J. Baró, P. Shyu, S. Pang, I. M. Jasiuk, E. Vives, E. K. Salje, and A. Planes, Avalanche criticality during compression of porcine cortical bone of different ages, Physical Review E **93**, 053001 (2016).
[23] S. Roux, A. Hansen, H. Herrmann, and E. Guyon, Rupture of heterogeneous media in the limit of infinite disorder, Journal of statistical physics **52**, 237 (1988).
[24] A. Hansen, E. L. Hinrichsen, and S. Roux, Scale-invariant disorder in fracture and related breakdown phenomena, Physical Review B **43**, 665 (1991).
[25] D. Sornette, Sweeping of an instability: an alternative to self-organized criticality to get power laws without parameter tuning, J. Phys. I **4**, 209 (1994).
[26] S. Zapperi, P. Ray, H. E. Stanley, and A. Vespignani, First-order transition in the breakdown of disordered media, Physical review letters **78**, 1408 (1997).
[27] S. Zapperi, P. Ray, H. E. Stanley, and A. Vespignani, Avalanches in breakdown and fracture processes, Physical Review E **59**, 5049 (1999).
[28] Y. Moreno, J. Gomez, and A. Pacheco, Fracture and second-order phase transitions, Physical review letters **85**, 2865 (2000).
[29] C. B. Picallo, J. M. López, S. Zapperi, and M. J. Alava, From brittle to ductile fracture in disordered materials, Physical Review Letters **105**, 155502 (2010).
[30] A. Shekhawat, S. Zapperi, and J. P. Sethna, From damage percolation to crack nucleation through finite size criticality, Physical review letters **110**, 185505 (2013).
[31] S. Biswas, S. Roy, and P. Ray, Nucleation versus percolation: Scaling criterion for failure in disordered solids, Physical Review E **91**, 050105 (2015).
[32] H. B. da Rocha and L. Truskinovsky, Rigidity-controlled crossover: From spinodal to critical failure, Physical Review Letters **124**, 015501 (2020).
[33] V. Kádár, Z. Danku, and F. Kun, Size scaling of failure strength with fat-tailed disorder in a fiber bundle model, Physical Review E **96**, 033001 (2017).
[34] S. Roy, S. Biswas, and P. Ray, Modes of failure in disordered solids, Physical Review E **96**, 063003 (2017).
[35] H. B. da Rocha and L. Truskinovsky, Mean field fracture in disordered solids: Statistics of fluctuations, Journal of the Mechanics and Physics of Solids **158**, 104646 (2022).
[36] C. D. Ferguson, W. Klein, and J. B. Rundle, Spinodals, scaling, and ergodicity in a threshold model with long-range stress transfer, Physical Review E **60**, 1359 (1999).
[37] O. E. Yewande, Y. Moreno, F. Kun, R. C. Hidalgo, and H. J. Herrmann, Time evolution of damage under variable ranges of load transfer, Physical Review E **68**, 026116 (2003).
[38] J. T. Kjellstadli, E. Bering, M. Hendrick, S. Pradhan, and A. Hansen, Can local stress enhancement induce stability in fracture processes? part i: Apparent stability, Frontiers in Physics **7**, 105 (2019).
[39] S. Sinha, S. Roy, and A. Hansen, Crack localization and the interplay between stress enhancement and thermal noise, Physica A: Statistical Mechanics and its Applications **569**, 125782 (2021).
[40] E. Berthier, A. Mayya, and L. Ponson, Damage spreading in quasi-brittle disordered solids: Ii. what the statistics of precursors teach us about compressive failure, Journal of the Mechanics and Physics of Solids **162**, 104826 (2022).
[41] A. Mayya, E. Berthier, and L. Ponson, How criticality meets bifurcation in compressive failure of disordered solids, Physical Review X (in press); arXiv:2207.12270 (2023).
[42] J. Weiss, L. Girard, F. Gimbert, D. Amitrano, and D. Vandembroucq, (finite) statistical size effects on compressive strength, Proceedings of the National Academy of Sciences **111**, 6231 (2014).
[43] V. Dansereau, V. Démery, E. Berthier, J. Weiss, and L. Ponson, Collective damage growth controls fault orientation in quasibrittle compressive failure, Physical review letters **122**, 085501 (2019).
[44] E. Berthier, V. Démery, and L. Ponson, Damage spreading in quasi-brittle disordered solids: I. localization and failure, Journal of the Mechanics and Physics of Solids **102**, 101 (2017).
[45] O. Narayan and D. S. Fisher, Threshold critical dynamics of driven interfaces in random media, Physical Review B **48**, 7030 (1993).
[46] K. J. Wiese, Theory and experiments for disordered elastic manifolds, depinning, avalanches, and sandpiles, Reports on Progress in Physics **85**, 086502 (2022).

[47] A. Mayya, E. Berthier, and L. Ponson, Procédé et dispositif d'analyse d'une structure. french patent application fr2002824 (2020).

[48] M. Kiyoo, Pressure dependence of rock strength and transition from brittle fracture to ductile flow, Bulletin of the Earthquake Research Institute **44**, 215 (1966).

[49] B. Evans, J. T. Fredrich, and T.-F. Wong, The brittle-ductile transition in rocks: Recent experimental and theoretical progress, The brittle-ductile transition in rocks **56**, 1 (1990).

[50] D. Amitrano, J.-R. Grasso, and D. Hantz, From diffuse to localised damage through elastic interaction, Geophysical research letters **26**, 2109 (1999).

[51] C. E. Renshaw and E. M. Schulson, Universal behaviour in compressive failure of brittle materials, Nature **412**, 897 (2001).

[52] D. Amitrano, Brittle-ductile transition and associated seismicity: Experimental and numerical studies and relationship with the b value, Journal of Geophysical Research: Solid Earth **108** (2003).

[53] J. Xue, S. Hao, J. Wang, F. Ke, C. Lu, and Y. Bai, The changeable power law singularity and its application to prediction of catastrophic rupture in uniaxial compressive tests of geomedia, Journal of Geophysical Research: Solid Earth **123**, 2645 (2018).

[54] A. Cartwright-Taylor, I. G. Main, I. B. Butler, F. Fusseis, M. Flynn, and A. King, Catastrophic failure: How and when? insights from 4-d in situ x-ray microtomography, Journal of Geophysical Research: Solid Earth **125**, e2020JB019642 (2020).

[55] J. Lemaitre, *A course on damage mechanics*, Amsterdam (Springer Verlag, 1992).

[56] G. Pijaudier-Cabot and Z. P. Bažant, Nonlocal damage theory, Journal of engineering mechanics **113**, 1512 (1987).

[57] J. Mazars and G. Pijaudier-Cabot, Continuum damage theory—application to concrete, Journal of engineering mechanics **115**, 345 (1989).

[58] K. Pham and J.-J. Marigo, From the onset of damage to rupture: construction of responses with damage localization for a general class of gradient damage models, Continuum Mechanics and Thermodynamics **25**, 147 (2013).

[59] B. Lawn, *Fracture of brittle solids* (Cambridge University Press, 1993).

[60] H. Gao and J. R. Rice, A first-order perturbation analysis of crack trapping by arrays of obstacles, Journal of Applied Mechanics **56**, 828 (1989).

[61] L. Ponson and N. Pindra, Crack propagation through disordered materials as a depinning transition: A critical test of the theory, Physical Review E **95**, 053004 (2017).

[62] A. Delaplace, G. Pijaudier-Cabot, and S. Roux, Progressive damage in discrete models and consequences on continuum modelling, Journal of the Mechanics and Physics of Solids **44**, 99 (1996).

[63] S. Pradhan, A. Hansen, and P. Ray, A renormalization group procedure for fiber bundle models, Frontiers in Physics **6**, 65 (2018).

[64] K. Pham, H. Amor, J.-J. Marigo, and C. Maurini, Gradient damage models and their use to approximate brittle fracture, International Journal of Damage Mechanics **20**, 618 (2011).

[65] R. Ince, A. Arslan, and B. Karihaloo, Lattice modelling of size effect in concrete strength, Engineering Fracture Mechanics **70**, 2307 (2003).

[66] G.-F. Zhao, J. Fang, and J. Zhao, A 3d distinct lattice spring model for elasticity and dynamic failure, International Journal for Numerical and Analytical Methods in Geomechanics **35**, 859 (2011).

[67] G. Pijaudier-Cabot and D. Grégoire, A review of non local continuum damage: Modelling of failure?, Networks & Heterogeneous Media **9**, 575 (2014).

[68] D. Kumar, A. Banerjee, and R. Rajesh, Interplay between disorder and hardening during tensile fracture of a quasi-brittle solid, Proceedings of the Royal Society A **478**, 20210934 (2022).

[69] B. Tyukodi, C. A. Lemarchand, J. S. Hansen, and D. Vandembroucq, Finite-size effects in a model for plasticity of amorphous composites, Physical Review E **93**, 023004 (2016).

[70] R. C. Hidalgo, Y. Moreno, F. Kun, and H. J. Herrmann, Fracture model with variable range of interaction, Physical review E **65**, 046148 (2002).

[71] J. Escartín, G. Hirth, and B. Evans, Nondilatant brittle deformation of serpentinites: Implications for mohr-coulomb theory and the strength of faults, Journal of Geophysical Research: Solid Earth **102**, 2897 (1997).

[72] O. Katz and Z. Reches, Microfracturing, damage, and failure of brittle granites, Journal of Geophysical Research: Solid Earth **109** (2004).

[73] T.-f. Wong and P. Baud, The brittle-ductile transition in porous rock: A review, Journal of Structural Geology **44**, 25 (2012).

[74] G. Hirth and J. Tullis, The brittle-plastic transition in experimentally deformed quartz aggregates, Journal of Geophysical Research: Solid Earth **99**, 11731 (1994).

[75] J. Vasseur, F. B. Wadsworth, M. J. Heap, I. G. Main, Y. Lavallée, and D. B. Dingwell, Does an inter-flaw length control the accuracy of rupture forecasting in geological materials?, Earth and Planetary Science Letters **475**, 181 (2017).

[76] J. Ritter, S. Shegufta, and M. Zaiser, Effects of disorder on deformation and failure of brittle porous materials, Journal of Statistical Mechanics: Theory and Experiment **2023**, 053301 (2023).

[77] A. Mayya, A. Banerjee, and R. Rajesh, Role of porosity and matrix behavior on compressive fracture of haversian bone using random spring network model, Journal of the Mechanical Behavior of Biomedical Materials **83**, 108 (2018).

[78] M. Pournajar, T. Mäkinen, S. A. Hosseini, P. Moretti, M. Alava, and M. Zaiser, Failure precursors and failure mechanisms in hierarchically patterned paper sheets in tensile and creep loading, arXiv preprint arXiv:2303.09214 (2023).

[79] Y. Xu, A. G. Borrego, A. Planes, X. Ding, and E. Vives, Criticality in failure under compression: Acoustic emission study of coal and charcoal with different microstructures, Physical Review E **99**, 033001 (2019).

[80] E. K. Salje, H. Liu, Y. Xiao, L. Jin, A. Planes, E. Vives, K. Xie, and X. Jiang, Avalanche mixing and the simultaneous collapse of two media under uniaxial stress, Physical Review E **99**, 023002 (2019).

[81] S. Senapati, A. Banerjee, and R. Rajesh, Role of composition in fracture behavior of two-phase solids, Physical Review E **107**, 055002 (2023).

[82] S. Bonfanti, E. E. Ferrero, A. L. Sellerio, R. Guerra, and S. Zapperi, Damage accumulation in silica glass nanofibers, Nano Letters **18**, 4100 (2018).